AGU PUBLICATIONS

Geochemistry, Geophysics, Geosystems

RESEARCH ARTICLE
10.1002/2014GC005270

Special Section:
The Lithosphere-asthenosphere System

Key Points:
- 3D Modeling of the Ordos Block using SINOPROBE magnetotelluric array dataset
- Conductor found beneath north Ordos suggests local lithosphere modification
- The modification may be relevant to the destruction of North China Craton

Correspondence to:
H. Dong,
donghao@cugb.edu.cn

Citation:
Dong, H., W. Wei, G. Ye, S. Jin, A. G. Jones, J. Jing, L. Zhang, C. Xie, F. Zhang, and H. Wang (2014), Three-dimensional electrical structure of the crust and upper mantle in Ordos Block and adjacent area: Evidence of regional lithospheric modification, *Geochem. Geophys. Geosyst.*, *15*, doi:10.1002/2014GC005270.

Received 28 JAN 2014
Accepted 9 MAY 2014
Accepted article online 16 MAY 2014

Three-dimensional electrical structure of the crust and upper mantle in Ordos Block and adjacent area: Evidence of regional lithospheric modification

Hao Dong[1,2], Wenbo Wei[1,2], Gaofeng Ye[1,2], Sheng Jin[1,2], Alan G. Jones[3], Jianen Jing[1,2], Letian Zhang[1], Chengliang Xie[1], Fan Zhang[1], and Hui Wang[1]

[1]School of Geophysics and Information Technology, China University of Geosciences, Beijing, China, [2]State Key Laboratory of Geological Processes and Mineral Resources, Beijing, China, [3]Dublin Institute for Advanced Studies, Dublin, Ireland

Abstract Long-period magnetotelluric (MT) data from project SINOPROBE were acquired and modeled, using three-dimensional (3D) MT inversion, to study the electrical structure of Ordos Block, a component of the North China Craton. For the first time, a high-resolution 3D resistivity model of the lithosphere is defined for the region. Contrary to what would be expected for a stable cratonic block, a prominent lithospheric conductive complex is revealed extending from the upper mantle to the mid-to-lower crust beneath the northern part of Ordos. Correlating well with results of seismic studies, the evidence from our independent magnetotelluric data supports regional modification of the lithosphere under the north Ordos and lithosphere thinning beneath Hetao Graben. The abnormally conductive structure may result from upwelling of mantle material in mid-to-late Mesozoic beneath the northern margin of the Ordos block.

1. Introduction

The Ordos Block (OB), which is located in the western part of the North China Craton (NCC), is one of the oldest and most stable cratonic blocks in Asia (Figure 1). After the amalgamation with the Yinshan Block (YB, Figure 1) along the Inner Mongolia Suture Zone (or Khondalite belt, IMSZ Figure 1) and the collision with the eastern part of the NCC at 1.8–1.9 Ga [*Zhao et al*., 2005; *Santosh*, 2010], the OB experienced a series of major tectonic events; Permo-Triassic suturing between the NCC and Mongolia [*Xiao et al*., 2003], collision between the NCC and the South China Craton in the Triassic [*Li et al*., 1993], and subduction of the Paleo-Pacific Plate initiating in the Cretaceous [*Griffin et al*., 1998]. According to seismology investigations, the present lithosphere of the east NCC is only ~60–100km thick [*Deng et al*., 2007; *An et al*., 2009]. Also, it is widely accepted that the lithosphere of the eastern part of NCC has been dramatic thinned in the late Mesozoic destruction/delamination process of the North China Craton [*Zhu et al*., 2012]. However, the OB is believed to have been largely unaffected by this process and to have preserved a seismically fast and thick lithospheric root of ~200 km [*Huang and Zhao*, 2006; *Li et al*., 2006; *Chen et al*., 2009]. Although few mantle xenoliths have been found within the OB, it is suggested that the OB retained a highly depleted cratonic mantle, according to analysis on Paleozoic kimberlite xenolith from Mengyin and Fuxian in eastern NCC [*Chu et al*., 2009] (Figure 1a).

Surrounded by a series of Cenozoic rift systems with intensive present-day seismic activity, the OB itself exhibits little seismicity and internal deformation today [*Deng et al*., 1999]. While little evidence of volcanic activity can be found within the OB, bounding rifts are abundant with different phases of volcanic rocks dated from Archean-Neoproterozoic to late Mesozoic [*Li and Gao*, 2010]. According to recent geothermal studies, the OB currently has an average geothermal gradient of ~29.7°C/km, and a heat flow of ~62 mW/m^2 [*Ren et al*., 2007], which is much higher than commonly found in Archean cratons of 40–50 mW/m^2 [*Pollack et al*., 1993]. Thinner lithosphere has been revealed beneath the north-bounding Hetao Graben (HG, Figure 1) and east-bounding Shanxi Graben (SG, Figure 1) by S-receiver function migration imaging [*Chen*, 2009] and body wave tomography [*Zhao et al*., 2012] around the OB.

Since electrical resistivity is essentially a transport property of the medium and is particularly sensitive to the presence of interconnected low-resistivity phases, such as partial melts or aqueous fluids, magnetotellurics (MT) has been frequently utilized to detect and image complex deep processes in the lithosphere resulting from fluids [e.g.,*Wei et al*., 2001; *Wannamaker et al*., 2009; *Bai et al*., 2010; *Kelbert et al*., 2012]. However,

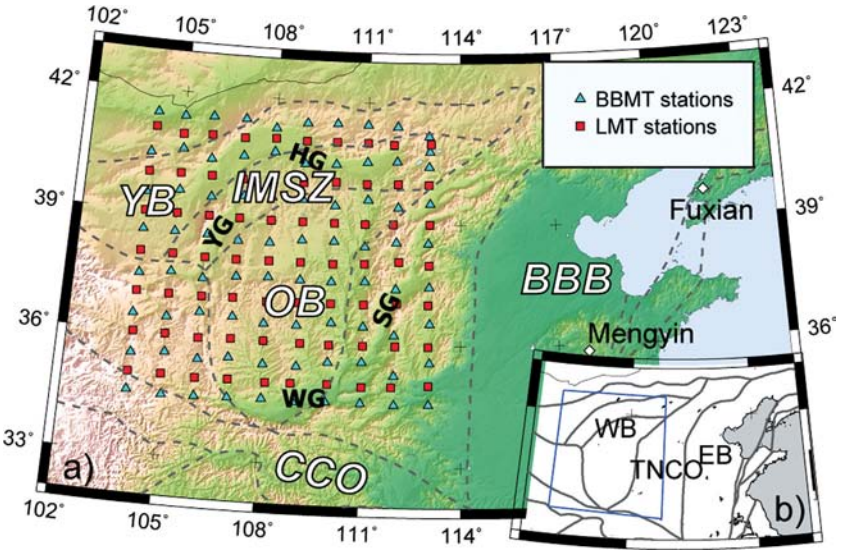

Figure 1. (a) MT site layout map superimposed on tectonic and topography map of North China. OB: Ordos Block, YB: Yinshan Block, BBB: Bohai Bay Basin, IMSZ: Inner Mongolia Suture Zone, CCO: Centre China Oregon, YG: Yinchuan Graben, HG: Hetao Graben, SG: Shanxi Graben, WG, Weihe Graben. The white diamonds show the locations of Kimberlite xenoliths in eastern NCC. (b) Simplified tectonic subdivision map of North China according to *Zhao et al.* [2001, 2005], the blue box shows the study area. WB: Western Block, EB: Eastern Block, TNCO: Trans-North China Oregon.

compared to the detailed velocity structure revealed by intensive seismic studies, the electrical structure of the OB and its adjacent area was not well studied. Previous MT studies, primarily broadband MT (BBMT), revealed crustal conductive layers in the west margin [*Wang et al*., 2010] and the central part of the OB [*Zhao et al*., 2011]. Conductive layers were also discovered in the upper mantle at 90–100 km on the northern margin of the OB [*Jiang et al*., 1990]. The previous MT studies in the region were mostly conducted as isolated short profiles, from which a comprehensive view was difficult to conclude for large-scale structures. Moreover, with the absence of long-period magnetotelluric (LMT) data, the depths of investigation of these studies were often limited to crustal scale. In this paper, we present the first 3D geoelectrical resistivity model of the crust and upper mantle in the Ordos Block and adjacent area, to aid further elucidation of the characteristics of the lithosphere in the region.

2. Magnetotelluric Data and Analysis

The MT time series data were acquired from 2010 to 2011 in the study region in a $1^\circ \times 1^\circ$ "standard grid network," which is a new multisite, facet-element MT survey scheme [W. Wei et al., Experiments of continental china magnetotelluric observation network and study on three-dimensional electrical structures of north china lithosphere, in preparation, 2014] used as standard in the SINOPROBE project [*Dong et al*., 2013]. Magnetotelluric data from a total of 693 broadband MT and 70 long-period MT sites were acquired in the study area using Phoenix MTU-5 BBMT and LVIV Lemi-417 LMT systems. In spite of the relatively low solar activity from 2010 to 2011, the MT data are generally of excellent quality free from electromagnetic noise in the western and middle part of the study area; some MT sites suffer from higher cultural noise effects in the eastern part. Most of the poor quality data lie in the period range of the so-called magnetotelluric dead band at 0.1–1 s where MT signal has a minimum signal-to-noise ratio. The time series were recorded synchronously at six BBMT sites and at three combined BBMT-LMT sites to facilitate remote reference processing [*Gamble et al*., 1979] in order to reduce the bias from incoherent noise. Electric and magnetic field time series were processed using a statistically robust algorithm [*Egbert and Booker*, 1986] to compute MT transfer functions in a period range of 0.01–1000 s (BBMT) and 10–10,000 s (LMT) respectively. However, some of the MT stations ($<$ 2%) suffered from strong coherent noise in the electrical channels, showing a typical 45 degree slope of the apparent resistivity curve of periods longer than 3s indicative of being in the near-field of a strong noise source; this noise could not be simply removed by the standard remote referencing scheme and the responses were omitted from further inversion scheme.

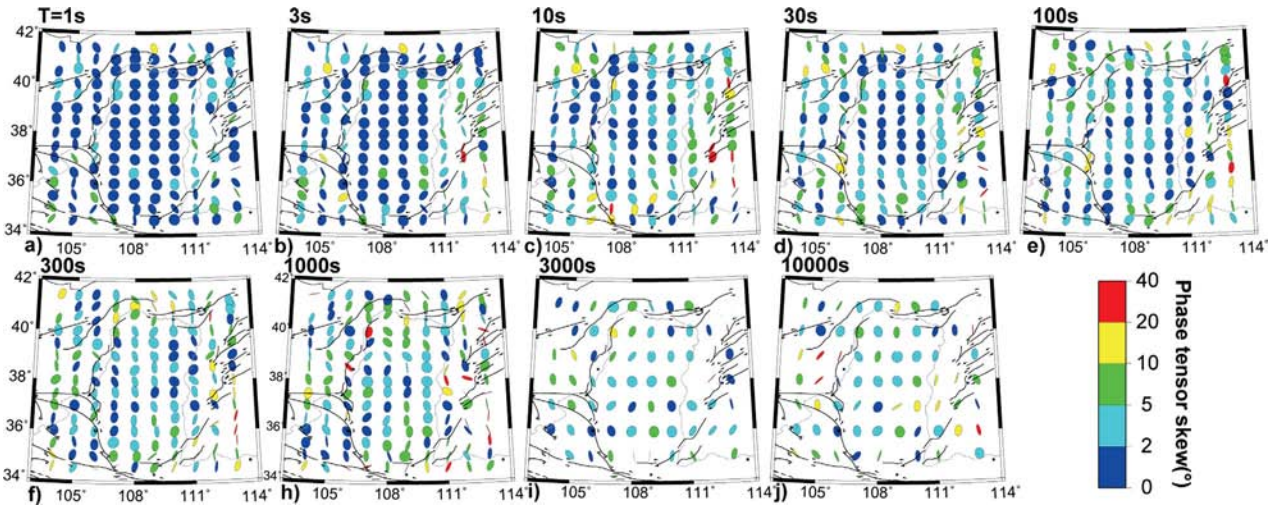

Figure 2. Geoelectrical phase tensor of the MT soundings at different periods of 1, 3, 10, 30, 100, 300, 1000, 3000, 10,000 s, superimposed by a map of fault system around Ordos. The colors filling the ellipses show the phase tensor skew angle β.

Figure 2 shows the geoelectrical MT phase tensors [*Caldwell et al*., 2004] at 1–10,000 s for the data used in the inversions. The orientations of phase tensor ellipses indicate the dominant flow direction of induced currents and reflect lateral resistivity variations of the subsurface structures; circular ellipses indicate one-dimensionality of the subsurface. The colors filling the phase tensor ellipses show the phase tensor skew angle β and indicate how three-dimensional (3D) the regional electrical structure is [*Caldwell et al*., 2004]. In the MT method, longer periods have more information about deeper structures; hence structure at different depths can be qualitatively inferred by phase tensors of different periods, although one must be cautious comparing neighboring sites due to differing penetration depths at the same period [e.g. *Hamilton et al*., 2006; *Jones*, 2011; *Miensopust et al*., 2011], and indeed the penetration depths in orthogonal directions may be completely different [*Jones*, 2006]. Anomalous ellipses and β values, compared to neighboring responses, are indicative of noise problems [*Jones*, 2012] and instabilities of the estimators in a similar manner to those of the rotational invariants due to their unbounded distributions [*Chave*, 2014]. At shorter periods of 1 s (Figure 2a), with an approximate average depth of penetration of 2–5 km, the circular phase tensors and small β values within the OB indicate an almost perfect 1D geoelectrical structure; this is consistent with the shallow structure of layered sediments in the OB. As period increases, the phase tensor ellipses display coherent N-S directions in the OB, indicating a strong N-S lateral conductivity gradient, whereas in the adjacent regions the orientations of the phase tensors approximately follow the rift structures (Figures 2d–2f). The increase of β values in the surrounding rift systems indicates the presence of 3D structures, calling for 3D interpretation methods; alternatively, in some cases, these high β values may indicate increasing noise levels on the impedance tensor estimates resulting in poor phase tensor estimates [*Jones*, 2012]. At longer periods ($>$ 1,000 s, Figures 2h–2j), the phase tensor ellipses become once again near-circular within the OB, from which decreased electrical heterogeneity can be inferred at greater depth.

3. 3D MT Inversion and Results

A 3D magnetotelluric inversion scheme WSINV3DMT [*Siripunvaraporn et al*., 2005] was employed for inversion of the data. Given the limitations of model mesh size and of data density possible for 3D inversion, the huge amount of data from the MT array network had to be reduced to manageable size for WSINV3DMT. In this study, only 150 out of 693 sounding sites were used for 3D inversion, including all 70 combined BBMT-LMT stations and 80 BBMT-only stations (Figure 1a). The BBMT-only stations were chosen to achieve an overall uniformly distributed station distribution to avoid under- or over-fitting of regional data. As shown in Figure 3, although admittedly some minor features are lost in the subset of data, major features are well retained even at the higher frequencies (Figure 3a). Full MT impedance tensor responses were inverted. A two-step inversion scheme for 3D inversion was utilized to avoid huge memory and CPU time consumption requirements. Twenty-four short periods in the band 0.01–100 s were used for the first-step, and the

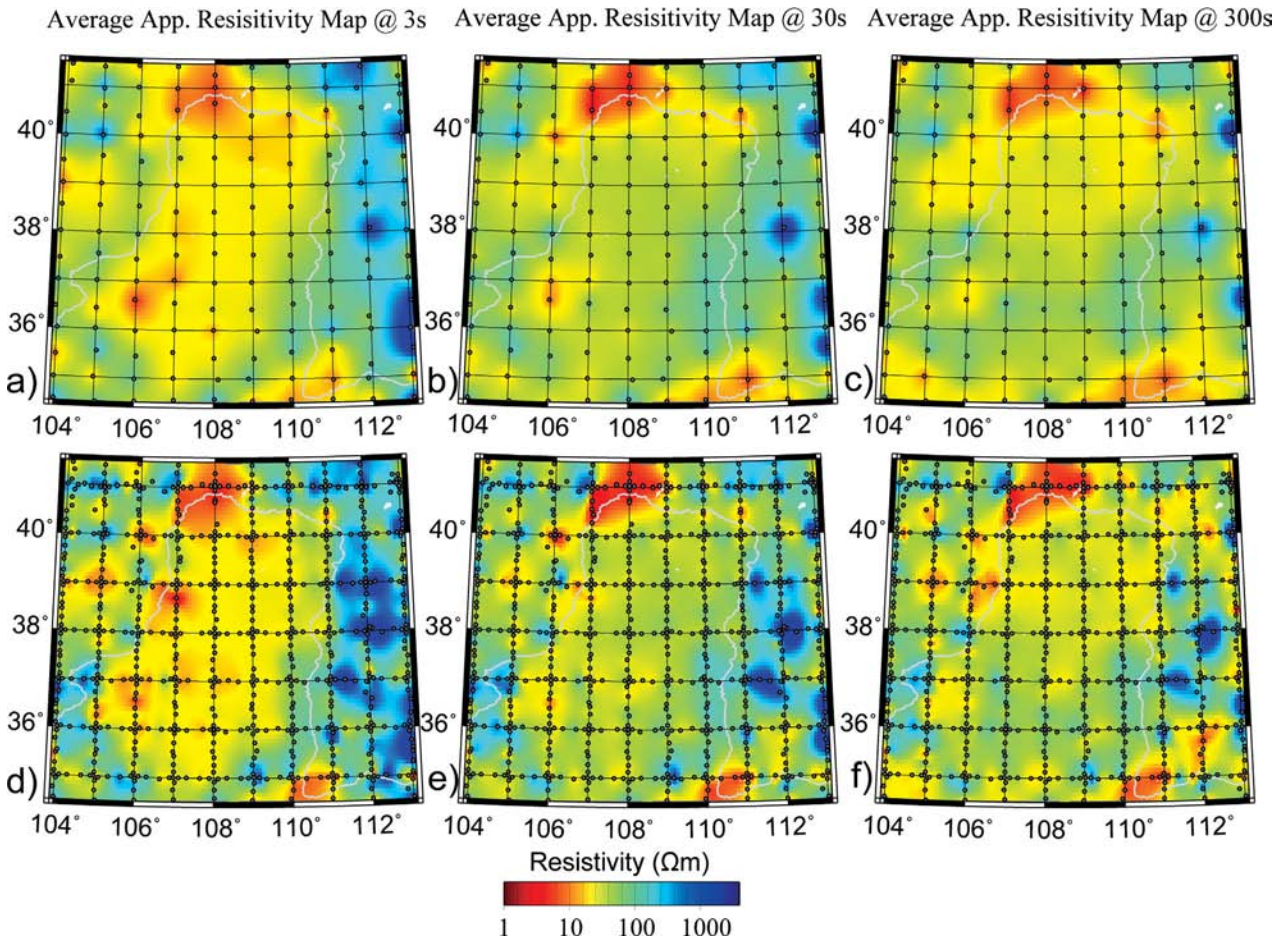

Figure 3. Horizontal maps of average apparent resistivity of the subdataset of 150 MT sites (a, b, c) and the full dataset of 693 sites (d, e, f) at 3, 30, and 300 s respectively.

resulting model was used as a starting model for the second step, which included a further 24 longer periods from 1 to 10,000 s.

Although the aim of the study is the deep structure, relatively high-frequency data (100 Hz, 0.01 s) and a thin uppermost model layer (20 m) was used in the study to allow the inversion scheme to generate minor (shallow) structures. This was done to partly simulate the local galvanic distortion or static shift [*Jones*, 2011]. Otherwise, the inversion scheme could generate deep artificial structures to "compensate" for local anomalies. In this study, the lower part of the model (>670 km) is set to be a conductive basement of 3 Ωm to ensure compliance with the lower boundary condition of the transition zone in mantle [*Booker et al*., 2004; *Kelbert et al*., 2009], while the upper part of the model is set to be a 100 Ωm layer as a starting model.

A series of "checkerboard" resolution tests were conducted to ascertain how well the model features could be recovered at different depths, as shown in Figure 4. The inversion grid and the site distribution used in the test were the same as for the field dataset. Three "layers" of checkerboards are included in the test, with a horizontal "block" dimension of 80 by 80 km and vertical thickness of 10 40, and 70 km (Figure 4a). A synthetic dataset, with 1% Gaussian noise of the impedance, was generated to test the two-step inversion scheme, and exactly the same procedures were followed (same sites, same periods, same starting models, same error floors, etc.). For the shallow structures, the checker board pattern is well resolved at 10 and 40 km (Figures 4b and 4c). As depth increases, the major features of the model could still be recovered at 120 km (Figure 4d), but with some smoothing and smearing due to model regularization and the reduction of MT stations with sufficient penetration depth. Conductive blocks are better resolved than resistive blocks, as expected for an EM induction method.

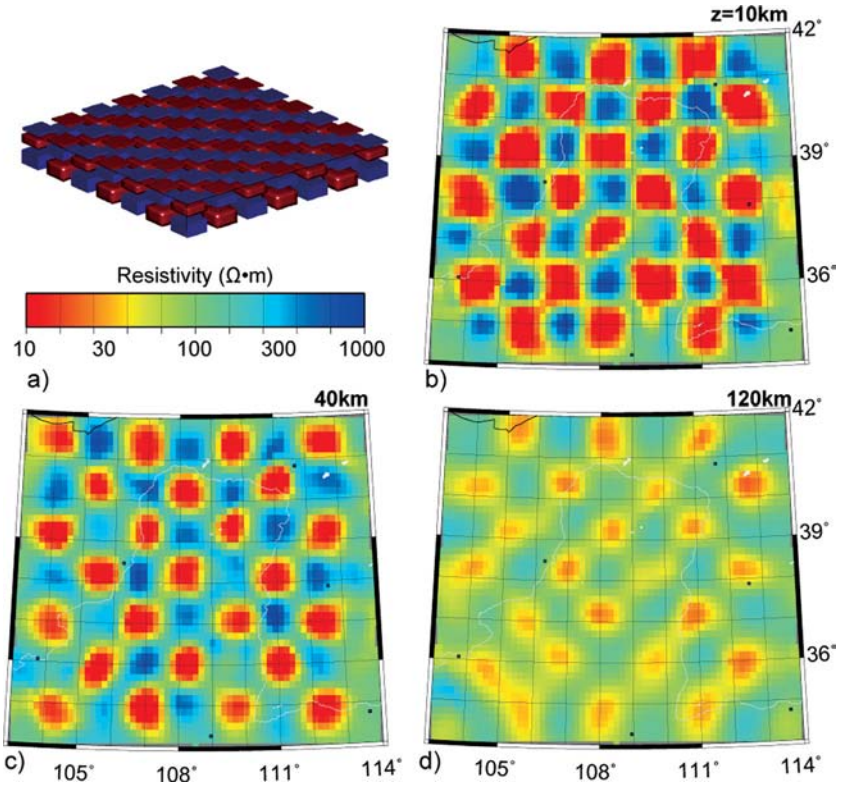

Figure 4. (a) Synthetic model used for forward calculation in the checkerboard test, see text for detail. (b-d) Horizontal slices of inversion result of the checkerboard test at 10, 40, and 120 km respectively.

The preferred inversion model (Figure 5) was achieved after eight iterations of the second step of the inversion, with a normalized RMS misfit of 1.60. As shown in Figures 6 and 7, the MT data are generally well fit, especially for the data within the OB.

As shown in the depth slices and sections of the final model (Figure 5), a large-scale highly conductive body C1 is revealed at depths of ~20–60 km, covering almost the entire northern part of the OB, as well as the Yinchuan Graben and Hetao Graben. In contrast to the resistive upper crust of ~300–1000 Ωm (Figures 5a and 5b), the resistivity of C1 ranges from several to tens of Ωm. The south part of the Ordos Block's lower crust is of moderate resistivity, ~100–300 Ωm, forming an electrical boundary along the latitude of 38°N, which explains the dominant N-S pattern of the phase tensor ellipses (Figures 2d–2f). A widespread conductive mantle electrical "basement," labeled C2, is revealed beneath the northern part of the Ordos Block and Hetao Graben, at a upper boundary varying from 90 km (beneath north margin of Ordos) to ~150 km (center of OB) and with a relatively low resistivity of 10–10 s of Ωm (Figures 5e and 5f). Just beneath the Inner Mongolia Suture Zone (IMSZ marked on Figures 1 and 5a), a vertical, south-dipping conductor, labeled C3, is imaged that connects the shallow conductive body C1 and the underlying body C2. C3 has a horizontal dimension of about 150 by 150 km and a resistivity of ~3–10 Ωm (Figures 5c and 5d).

Due to the diffusive propagation of the electromagnetic signal within conductive layers, the MT method has inherent difficulties recovering structures beneath a conductive structure (see, e.g., *Jones* [1999] and *Schwalenberg et al*. [2002]). To test the sensitivity of the MT data to the presence of conductor C3 under C1, a forward model was computed with C3 replaced by resistivity of 300 Ωm at 50–90 km depth (Figures 8a and 8b). While removing C3 had a relatively minor impact on the overall misfit (normalize RMS changed from 1.60 to 1.66), a ~10–20 % change was produced in responses among corresponding periods at sites the boundaries anomaly (Figures 8c–8e), suggesting that C3 is well constrained by the MT data. This also exemplifies that RMS is a poor measure of model fit for specific features in the data, as discussed and illustrated by *Jones* [1993]. It should be noted that only the stations around C3 show the major changes of the response (see the station location in Figure 8a) as the stations right above C3 see little change as their depth penetration is limited by the existence of C3 itself.

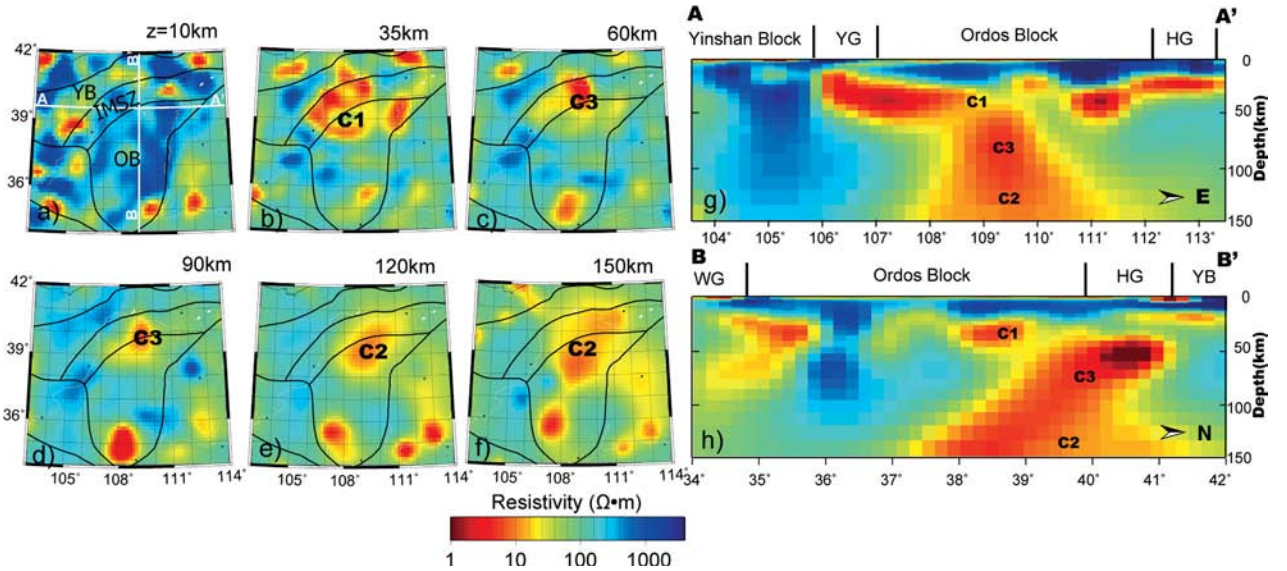

Figure 5. (a-f) Horizontal resistivity map of the preferred inversion model at depths of 10, 35, 60, 90, 120, and 150 km, superimposed with tectonic division according to *Zhao et al.* [2001, 2005].(g and h) Resistivity section of the preferred inversion model along the profile A-A′ and B-B′ (see Figure 5a for profile location). See caption of Figure 1 for the abbreviations of tectonic units.

4. Discussion

One of the most striking features of our inverse result is the large-scale conductor C1 in the lower crust to upper mantle beneath the north Ordos Block and the Hetao Graben (Figures 5b, 5h, and 5g). While the

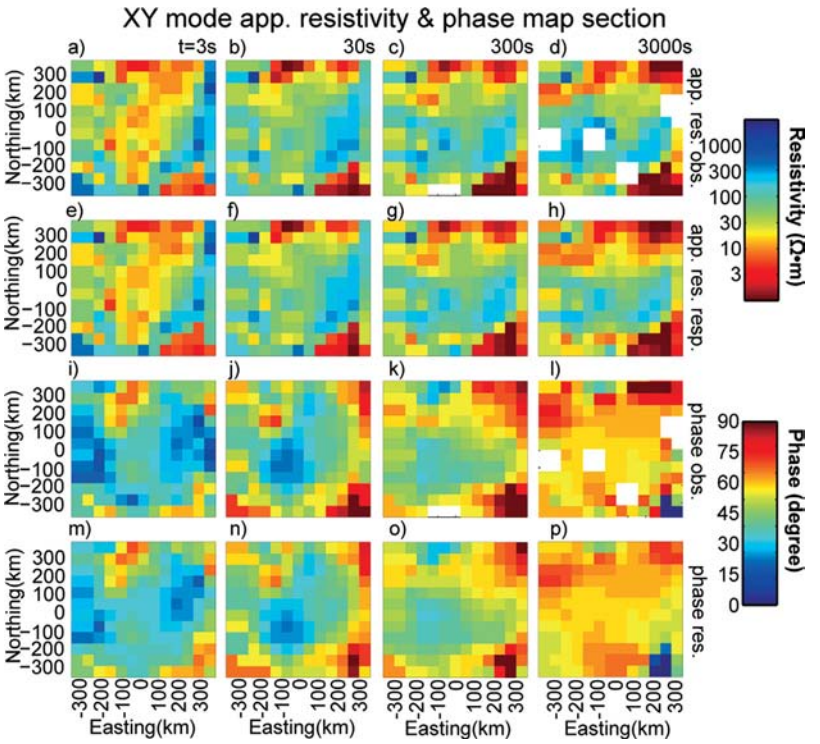

Figure 6. Horizontal maps of XY mode of observed and response MT data for merged broadband and long-period data from 150 sites in Ordos data set. Note the data are regularized so as to plot on uniform grids.(a-d) Observed apparent resistivity maps at 3, 30, 300, and 3000 s. (e-h) Response apparent resistivity maps at 3, 30, 300, and 3000 s. (i-l) Observed impedance phase maps at 3, 30, 300, and 3000 s. (m-p) Response impedance phase maps at 3, 30, 300, and 3000 s.

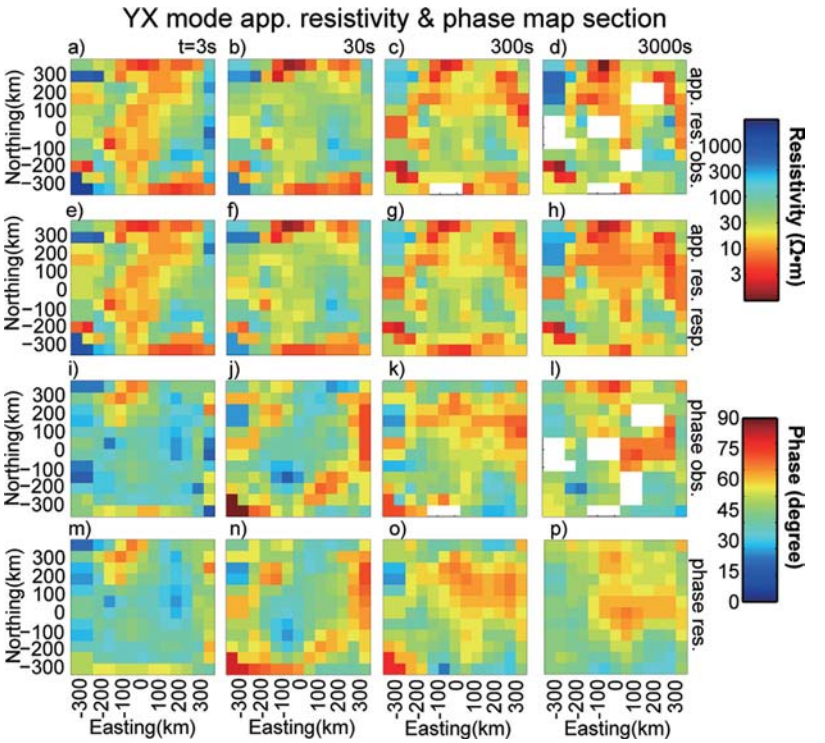

Figure 7. Horizontal maps of YX mode of observed and response MT data for merged broadband and long-period data from 150 sites in Ordos dataset. Note the data are regularized so as to plot on uniform grids. (a-d) Observed apparent resistivity maps at 3, 30, 300, and 3000 s. (e-h) Response apparent resistivity maps at 3, 30, 300, and 3000 s. (i-l) Observed impedance phase maps at 3, 30, 300, and 3000 s. (m-p) Response impedance phase maps at 3, 30, 300, and 3000 s.

upper boundary and resistivity of C1 are consistent with the in-crust conductor revealed by previous MT studies [*Zhao et al*., 2011], our model has superior constraints on its lower boundary, due to the greater spatial extent of our stations and the greater penetration depths of the new LMT data. Another fascinating feature of the derived 3D resistivity model is the vertical conductor C3 rising from the large-scale upper mantle conductive body C2 and penetrating north to the base of C1 (Figures 5c–5h). As shown in Figure 9a, an up to 3% low shear velocity (Vs) zone beneath the northern margin of OB, identified by body wave [*Zhao et al*., 2009] and surface wave tomography [*Huang et al*., 2009; *Jiang et al*., 2013], is coincident with the location of C2 and C3 (Figure 9b), but with greater depth and a smaller horizontal scale.

Hence a question arises as to what is the cause of this massive mushroom-shaped high conductivity complex? High conductivity anomalies and structures in the crust and upper mantle have been frequently observed in many parts of the world, and have long been an enigma that needs to be addressed (for the lower crust, e.g., *Jones* [1992]). These conductive structures are often interpreted as various mechanisms, such as partial melts [*Wei et al*., 2001; *Kelbert et al*., 2012], graphite/sulphide [*Jones*, 1993; *Jones et al*., 2003], iron oxides [*Duba et al*., 1994], aqueous (saline) fluids [*Nesbritt*, 1993; *Marquis et al*., 1995; *Bai et al*., 2010; *Zhao et al*., 2011], hydrogen diffusion in olivine in the mantle [*Karato*, 1990; *Jones et al*., 2012, 2013], or a combination of some or all of the above [*Duba et al*., 1994; *Wannamaker et al*., 2008].

For the lower crust and uppermost mantle conductor C1, most of it lies within the stable and seismically fast [*Teng et al*., 2010] Ordos Block. With remarkable spatial coincidence with C1 in this study, a high Vp/Vs ratio zone was revealed in the lower crust of the region by recent studies of P wave receiver functions [*Tian et al*., 2011]. A high Vp/Vs ratio of 1.80 was observed, in contrast with a normal value of 1.75 in the center part of the OB, indicating a lower crust of low viscosity; this could imply the presence of fluids [*Zhang et al*., 2009]. For the partial melt hypothesis, given the current heat flow of Ordos Block ($\sim$62 mW/m^2) [*Ren et al*., 2007], the lower crust can be interpreted to have a moderate temperature of about 400–600°C [*Zang et al*., 2005], which does not facilitate partial melting, even in wet conditions. As for aqueous fluids, at the conditions of the lower crust, with a saline fluid resistivity of 20 S/m, a small amount ($<$5 %) of interconnected

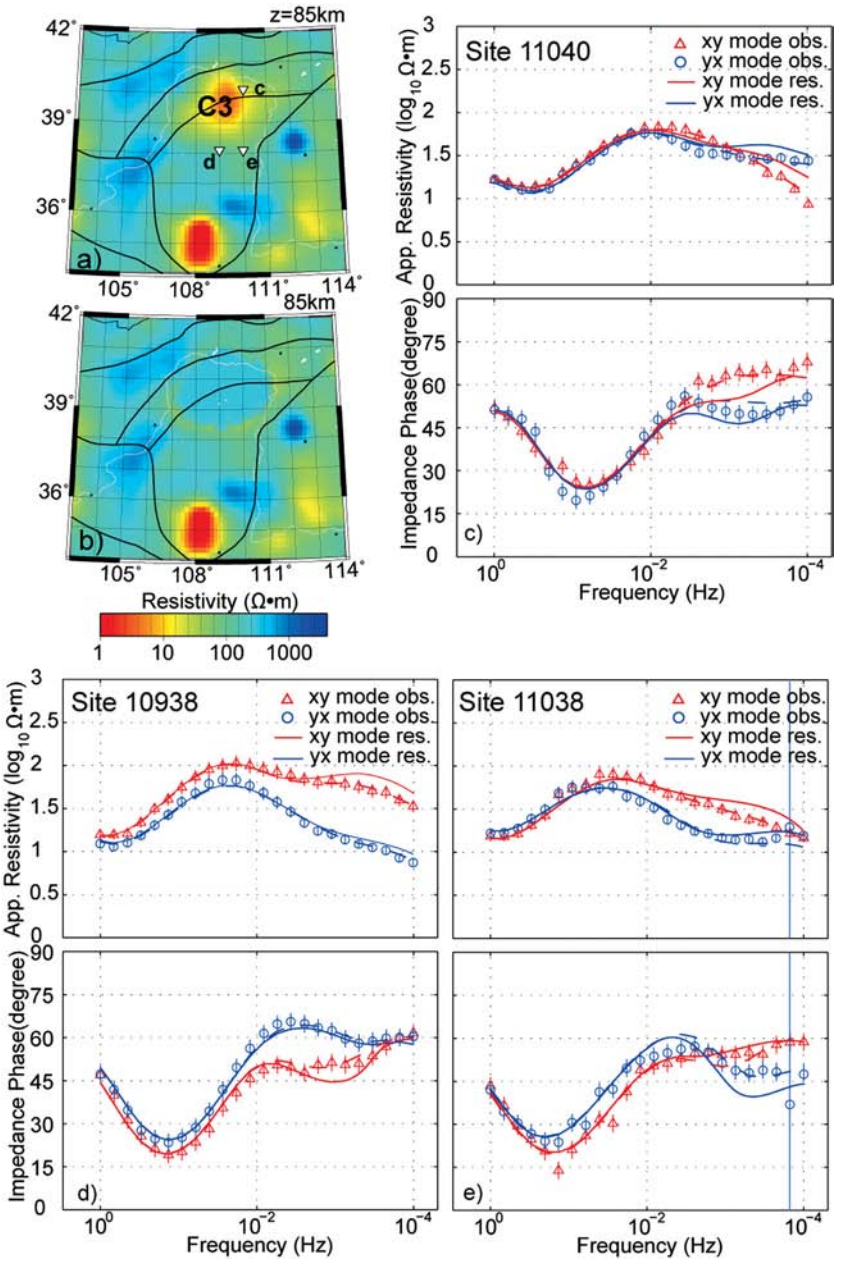

Figure 8. Comparisons of models and MT responses in sensitivity tests of the conductor C3. (a) Map section of the original preferred inversion model at 85 km depth. The inverted triangles indicate the locations of the corresponding stations in Figures 8c(11040), 8d(10938), and 8e(11038). (b) Map section of the modified inversion model at 85 km depth. (c-e) MT data and responses from station 11040, 10938, and 11038. The solid lines indicate the response of modified model, whereas the dashed lines show the response of original model.

fluid phase is sufficient to produce a resistivity as observed in C1 [*Nesbritt*, 1993; *Li et al*., 2003]. For the graphites/sulphides alternative, while graphite minerals would not explain the high Vp/Vs observed, sulphides have been reported to have a high Vp/Vs ratio up to 1.90 [*Ludwig et al*., 1998].

For the deeper conductive structures in the mantle, C2 and C3, interpretation is far more complicated due to the lack of thermal and compositional constraints from mantle xenoliths within the OB. For anomaly C2, which lies mostly below the inferred thermal lithosphere boundary [*Zang et al*., 2005], a low resistivity of ~10 Ωm could be produced with a ~1–2 wt% basaltic melt in the olivine system [*Yoshino et al*., 2010]. However, such a melt proportion would cause a >6% Vs reduction [*Hammond and Humphreys*, 2000], which is not allowed by the seismic data. The low resistivity could also be explained by high water content (~1000 ppm) inducing hydrogen diffusion in olivine [*Wang et al*., 2006]; such water contents are not visible in

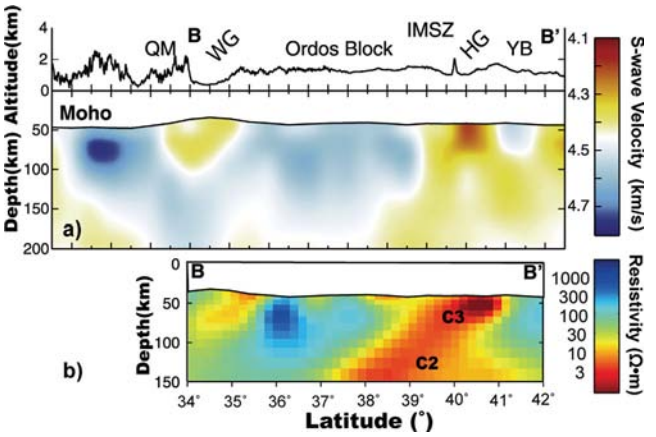

Figure 9. Comparison of S-wave velocity and resistivity sections along profile B-B′, see Figure 7a for the profile location. YB: Yinshan Block, IMSZ: Inner Mongolia Suture Zone, HG: Hetao Graben, WG, Weihe Graben, QM: Qinling Mountains. Note the resistivity section above Moho is masked as in the S-wave velocity section for better comparison. (a) S-wave velocity section along the profile B-B′ (Modified from *Jiang et al.* [2013]) (b) Resistivity section of the preferred inversion model along the profile B-B′.

seismic velocities. However, this conjecture is inadmissible as the maximum bulk water storage capability should be around 190 ppm in the upper mantle [*Kovács et al.*, 2012]. Alternately, a very low fraction (0.1%) of interconnected carbonititic melt in the olivine matrix would also provide the low resistivity observed [*Gaillard et al.*, 2008] and would not have an observable seismic response.

For the shallower anomaly C3, one may appeal to a small fraction (> 4 vol %) of silicate melt in the upper mantle [*Partzsch et al.*, 2000] for the cause of low resistivity as well as low versus velocity. The sulphides hypothesis, on the other hand, could still be valid for both C2 and C3, as in the case of what is proposed to explain the low resistivities associated with the Bushveld complex in the Kaapvaal Craton [*Evans et al.*, 2011]. However, we have no evidence for the presence or absence of sulphides within the lithospheric mantle of the OB.

According to paleogeothermal research, the Ordos Block has experienced a much higher geothermal gradient than today [*Sun and Liu*, 1996; *Ren et al.*, 2007]. Various techniques, such as apatite fission track, fluid inclusions, and vitrinite reflectance, show that the northern part of OB might have had a geothermal gradient as high as ~45°C/km in the late Mesozoic [*Ren*, 1996; *Yuan et al.*, 2007]. At around 100 Ma, an abrupt heat flow increase in the Ordos Block is revealed by the vitrinite reflectance analysis with sedimentation from oil and gas wells [*Jiao et al.*, 2013]. The heat flow of OB rose from 40 to 50 mW/m^2 to a peak of about 80 mW/m^2 and slowly reduced to the present day level. Considering the thermal conduction time from the upper mantle to the surface, the major thermal-tectonic event may have started as early as the Jurassic. In that case, the aqueous fluids explanation seems less convincing, since aqueous fluids do not survive for the relatively long geological timescales (>100 Ma). Hence conducting sulphides might be a more favorable and

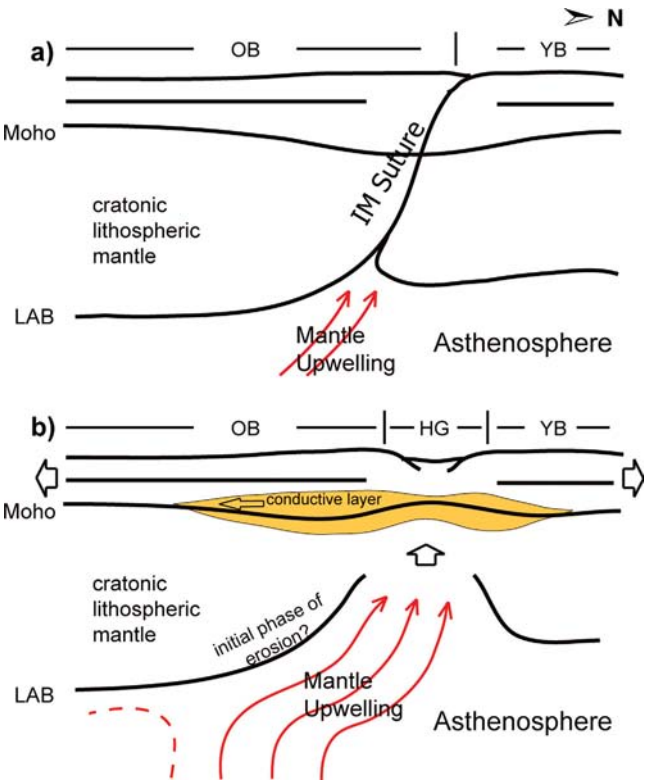

Figure 10. Schematic illustration of dynamic processes of the study region. See caption of Figure 1 for the abbreviations of tectonic units.

consistent mechanism for C1, C2 as well as C3. As the time of the thermal event coincides with the destruction of the NCC in the late Mesozoic, it is highly likely that the process of destruction of the NCC also affected and induced a partial modification of the Ordos Craton.

Figure 10 shows a schematic cartoon of our interpretation of the geoelectrical model presented above. In this scenario, possibly induced by the subduction of Paleo-Pacific Plate, hot upwelling material started to rise from the upper mantle in the mid-to-late Mesozoic. Encountering the stable cratonic lithospheric root of the Ordos Block, the buoyant mantle material had to find a weaker part of the lithosphere to continue rising (Figure 10a). Therefore, through the south-dipping suture zone of IMSZ between the OB and the YB [*Santosh*, 2010], the upwelling material rose to the north, introduced sulphides and/or carbonatites/silicate melts to the channel and modifying the regional lithosphere. The upwelling material could also have brought sulphides laterally to the lower crust and uppermost mantle of the OB, inducing the low resistivity and high Vp/Vs anomaly in C1 (Figure 10b). The hot material could as well have induced the Yanshanian (Jurassic to Cretaceous) volcanic activity on the north margin of Ordos and contribute to the abrupt heat flow increasing to north Ordos in late Mesozoic. Moreover, the upwelling could also contribute to the extension of the Hetao Graben started in the late Tertiary as well as the uplifting of the north the Ordos Block since the Neogene [*Zhang et al*., 1998; *Tian et al*., 2011].

What we discussed above are just the most plausible mechanisms that could generate the low resistivity anomaly in the region. Therefore, additional constraints are required to better study the deep processes in the region, calling for further investigations.

5. Conclusions

A high-resolution electrical resistivity model of the Ordos Block (OB) and its bounding areas was obtained using 3D inversion modeling of high-quality MT data acquired on a regular grid. The lithosphere beneath the northern part of the OB and Hetao Graben is geoelectrically distinct from that beneath the stable middle and southern Ordos. Compelling evidence is presented of a large-scale conductive complex in the lower crust and upper mantle beneath north OB and the Hetao Graben. Such lithospheric mantle low resistivity anomalies have been found in other cratons worldwide, including the Slave Craton [*Jones et al*., 2003], the Sask Craton [*Jones et al*., 2005] the western part of the Superior Craton [*Ferguson et al*., 2005], and the part of the Kaapvaal Craton modified by Bushveld magmatism [*Evans et al*., 2011]. Although the candidates to explain these mid-lithospheric anomalies are many, in the case of the Ordos Block by elimination and through consideration of the coincident velocity anomaly, we conclude that the reduced resistivity possibly results from a mechanism involving sulphides. While questions remain, the evidence from magnetotelluric data suggests an upwelling of mantle material beneath the IMSZ in the late Mesozoic, and that upwelling introduced fluids into the upper lithospheric mantle that deposited sulphides. While the lithospheric root of the Ordos Block appears to be largely intact, based on seismic studies, it may have experienced regional modification and lithosphere thinning beneath the northern margin of Ordos and the Hetao Graben in the late Mesozoic process of destruction of North China Craton.

Acknowledgments

This study is supported by project SINOPROBE [*Dong et al*., 2013] on sub-project SINOPROBE 01-02 and 01-01. The authors want to express gratitude to Professor Weerachai Siripunvaraporn to make his code WSINV3DMT available to the research community. Also we would like to extend our gratitude to the valuable reviews from our anonymous reviewer. Special thanks must go to the field crews and students; without them, this study could never be accomplished.

References

An, M., M. Feng, and Y. Zhao (2009), Destruction of lithosphere within the North China Craton inferred from surface wave tomography, *Geochem. Geophys. Geosyst.*, *10*, Q08016, doi:10.1029/2009GC002562.

Bai, D., et al. (2010), Crustal deformation of the eastern Tibetan plateau revealed by magnetotelluric imaging, *Nat. Geosci.*, *3*(5), 358–362, doi:10.1038/ngeo830.

Booker, J., A. Favetto, and M. Pomposiello (2004), Low electrical resistivity associated with plunging of the Nazca flat slab beneath Argentina, *Nature*, *429*, 399–403, doi:10.1038/nature02573.1.

Caldwell, T. G., H. M. Bibby, and C. Brown (2004), The magnetotelluric phase tensor, *Geophys. J. Int.*, *158*(2), 457–469, doi:10.1111/j.1365-246X.2004.02281.x.

Chave, A. D. (2014), On the statistics of magnetotelluric rotational invariants, *Geophys. J. Int.*, *196*(1), 111–130, doi:10.1093/gji/ggt366.

Chen, L. (2009), Lithospheric structure variations between the eastern and central North China Craton from S- and P-receiver function migration, *Phys. Earth Planet. Inter.*, *173*(3-4), 216–227, doi:10.1016/j.pepi.2008.11.011.

Chen, L., C. Cheng, and Z. Wei (2009), Seismic evidence for significant lateral variations in lithospheric thickness beneath the central and western North China Craton, *Earth Planet. Sci. Lett.*, *286*(1-2), 171–183, doi:10.1016/j.epsl.2009.06.022.

Chu, Z.-Y., F.-Y. Wu, R. J. Walker, R. L. Rudnick, L. Pitcher, I. S. Puchtel, Y.-H. Yang, and S. a. Wilde (2009), Temporal evolution of the lithospheric mantle beneath the eastern North China Craton, *J. Petrol.*, *50*(10), 1857–1898, doi:10.1093/petrology/egp055.

Deng, J., S. Su, Y. Niu, C. Liu, G. Zhao, X. Zhao, S. Zhou, and Z. Wu (2007), A possible model for the lithospheric thinning of North China Craton: Evidence from the Yanshanian (Jura-Cretaceous) magmatism and tectonism, *Lithos*, *96*(1-2), 22–35, doi:10.1016/j.lithos.2006.09.009.

Deng, Q. D., S. P. Cheng, W. Min, G. Z. Yang, and D. W. Ren (1999), Discussion on Cenozoic tectonics and dynamics of Ordos Block, *J. Geomech.*, *5*(3), 12–21.
Dong, S.-W., T.-D. Li, Q.-T. Lü, R. Gao, J.-S. Yang, X.-H. Chen, W.-B. Wei, and Q. Zhou (2013), Progress in deep lithospheric exploration of the continental China: A review of the SinoProbe, *Tectonophysics*, *606*, 1–13, doi:10.1016/j.tecto.2013.05.038.
Duba, A., S. Heikamp, W. Meurer, G. Mover, and G. Will (1994), Evidence from borehole samples for the role of accessory minerals in lower-crustal conductivity, *Nature*, *367*(6458), 59–61, doi:10.1038/367059a0.
Egbert, G. D., and J. R. Booker (1986), Robust estimation of geomagnetic transfer functions, *Geophys. J. Int.*, *87*(1), 173–194.
Evans, R. L., et al. (2011), Electrical lithosphere beneath the Kaapvaal craton, southern Africa, *J. Geophys. Res.*, *116*, B04105, doi:10.1029/2010JB007883.
Ferguson, I. J., J. A. Craven, R. D. Kurtz, D. E. Boerner, R. C. Bailey, X. Wu, M. R. Orellana, J. Spratt, G. Wennberg, and M. Norton (2005), Geoelectric response of Archean lithosphere in the western Superior Province, central Canada, *Phys. Earth Planet. Inter.*, *150*(1-3), 123–143, doi:10.1016/j.pepi.2004.08.025.
Gaillard, F., M. Malki, G. Iacono-Marziano, M. Pichavant, and B. Scaillet (2008), Carbonatite melts and electrical conductivity in the asthenosphere., *Science*, *322*(5906), 1363–1365, doi:10.1126/science.1164446.
Gamble, T., W. Goubau, and J. Clarke (1979), Error analysis for remote reference magnetotellurics, *Geophysics*, *44*(5), 959–968.
Griffin, W., A. Zhang, S. O'reilly, and C. Ryan (1998), Phanerozoic evolution of the lithosphere beneath the Sino-Korean Craton, in *Mantle Dynamics and Plate Interactions in East Asia, Geodynamic Ser.*, vol. 27, edited by S. L. Hung, C. H. Lo, and T. Y. Lee, pp. 107–126, AGU, Washington, D. C.
Hamilton, M. P., A. G. Jones, R. L. Evans, S. Evans, C. J. S. Fourie, X. Garcia, A. Mountford, and J. E. Spratt (2006), Electrical anisotropy of South African lithosphere compared with seismic anisotropy from shear-wave splitting analyses, *Phys. Earth Planet. Inter.*, *158*(2-4), 226–239, doi:10.1016/j.pepi.2006.03.027.
Hammond, W. C., and E. D. Humphreys (2000), Upper mantle seismic wave velocity' Effects of realistic partial melt geometries, *J. Geophys. Res.*, *105*(B5), 10975–10986.
Huang, J., and D. Zhao (2006), High-resolution mantle tomography of China and surrounding regions, *J. Geophys. Res.*, *111*, B09305, doi:10.1029/2005JB004066.
Huang, Z., H. Li, Y. Zheng, and Y. Peng (2009), The lithosphere of North China Craton from surface wave tomography, *Earth Planet. Sci. Lett.*, *288*(1-2), 164–173, doi:10.1016/j.epsl.2009.09.019.
Jiang, M., Y. Ai, L. Chen, and Y. Yang (2013), Local modification of the lithosphere beneath the central and western North China Craton: 3-D constraints from Rayleigh wave tomography, *Gondwana Res.*, *24*(3-4), 849–864, doi:10.1016/j.gr.2012.06.018.
Jiang, Z., J. Sun, and C. Xu (1990), Preliminary study on the conductivity structure of the crust and upper mantle: Third report on the geoscience transect from Xiangshui, Jiangsu-Mandula, Neimenggu, *Seismol. Geol.*, *12*(3), 193–206.
Jiao, Y., N. Qiu, W. Li, Y. Zuo, Y. Que, and F. Liu (2013), The Mesozoic-Cenozoic evolution of lithosphere thickness in the Ordos basin constrained by geothermal evidence, *Chin. J. Geophys.*, *56*(9), 3051–3060.
Jones, A. G. (1992), Electrical conductivity of the continental lower crust, in *Continental Lower Crust*, edited by D. M. Fountain, R. J. Arculus, and R. W. Kay, pp. 81–143, Elsevier B.V.
Jones, A. G. (1993), Electromagnetic images of modern and ancient subduction zones, *Tectonophysics*, *219*, 29–45.
Jones, A. G. (1999), Imaging the continental upper mantle using electromagnetic methods, *Lithos*, *48*(1-4), 57–80, doi:10.1016/S0024-4937(99)00022-5.
Jones, A. G. (2006), Electromagnetic interrogation of the anisotropic Earth: Looking into the Earth with polarized spectacles, *Phys. Earth Planet. Inter.*, *158*(2-4), 281–291, doi:10.1016/j.pepi.2006.03.026.
Jones, A. G. (2011), Three-dimensional galvanic distortion of three-dimensional regional conductivity structures: Comment on "Three-dimensional joint inversion for magnetotelluric resistivity and static shift distributions in complex media" by Yutaka Sasaki and Max A. Meju, *J. Geophys. Res.*, *116*, B12104, doi:10.1029/2011JB008665.
Jones, A. G. (2012), Distortion of magnetotelluric data: Its identification and removal., in *The Magnetotelluric Method: Theory and Practice*, edited by A. D. Chave and A. G. Jones, Cambridge Univ. Press., Cambridge, U. K.
Jones, A. G., P. Lezaeta, I. J. Ferguson, A. D. Chave, R. L. Evans, X. Garcia, and J. Spratt (2003), The electrical structure of the Slave craton, *Lithos*, *71*(2-4), 505–527, doi:10.1016/j.lithos.2003.08.001.
Jones, A. G., J. Ledo, and I. J. Ferguson (2005), Electromagnetic images of the Trans-Hudson orogen: The North American Central Plains anomaly revealed, *Can. J. Earth Sci.*, *42*(4), 457–478, doi:10.1139/e05–018.
Jones, A. G., J. Fullea, R. L. Evans, and M. R. Muller (2012), Water in cratonic lithosphere: Calibrating laboratory-determined models of electrical conductivity of mantle minerals using geophysical and petrological observations, *Geochem. Geophys. Geosyst.*, *13*, Q06010, doi:10.1029/2012GC004055.
Jones, A. G., S. Fishwick, R. L. Evans, M. R. Muller, and J. Fullea (2013), Velocity-conductivity relations for cratonic lithosphere and their application: Example of Southern Africa, *Geochem. Geophys. Geosyst.*, doi:10.1002/ggge.20075, in press.
Karato, S. (1990), The role of hydrogen in the electrical conductivity of the upper mantle, *Nature*, *347*, 272–273.
Kelbert, A., A. Schultz, and G. Egbert (2009), Global electromagnetic induction constraints on transition-zone water content variations., *Nature*, *460*(7258), 1003–6, doi:10.1038/nature08257.
Kelbert, A., G. D. Egbert, and C. DeGroot-Hedlin (2012), Crust and upper mantle electrical conductivity beneath the Yellowstone Hotspot Track, *Geology*, *40*(5), 447–450, doi:10.1130/G32655.1.
Kovács, I., D. H. Green, A. Rosenthal, J. Hermann, H. S. C. O'neill, W. O. Hibberson, and B. Udvardi (2012), An experimental study of water in nominally anhydrous minerals in the upper mantle near the water-saturated solidus, *J. Petrol.*, *53*(10), 2067–2093, doi:10.1093/petrology/egs044.
Li, C., R. D. van der Hilst, and M. N. Toksöz (2006), Constraining P-wave velocity variations in the upper mantle beneath Southeast Asia, *Phys. Earth Planet. Inter.*, *154*(2), 180–195, doi:10.1016/j.pepi.2005.09.008.
Li, M., and J. Gao (2010), Basement faults and volcanic rock distributions in the Ordos Basin, *Sci. China Earth Sci.*, *53*(11), 1625–1633, doi:10.1007/s11430-010-4042-8.
Li, S., Y. Xiao, D. Liou, Y. Chen, N. Ge, and Z. Zhang (1993), Collision of the North China and Yangtse Blocks and formation of coesite-bearing eclogites: Timing and processes, *Chem. Geol.*, *109*(1–4), 89–111.
Li, S., M. Unsworth, and J. R. Booker (2003), Partial melt or aqueous fluid in the mid-crust of Southern Tibet? Constraints from INDEPTH magnetotelluric data, *Geophys. J. Int.*, *153*, 289–304.
Ludwig, R. J, G. J. Iturrino, and P. A. Rona (1998), Seismic velocity-porosity relationship of sulfide, sulfate, and basalt samples from the tag hydrothermal mound, in Proceedings of the Ocean Drilling Program: Scientific Results, vol. 158, pp 313–327.

Marquis, G., A. G. Jones, and R. D. Hyndman (1995), Coincident conductive and reflective middle and lower crust in southern British Columbia, *Geophys. J. Int.*, *120*(1), 111–131, doi:10.1111/j.1365-246X.1995.tb05915.x.

Miensopust, M. P., A. G. Jones, M. R. Muller, X. Garcia, and R. L. Evans (2011), Lithospheric structures and Precambrian terrane boundaries in northeastern Botswana revealed through magnetotelluric profiling as part of the Southern African Magnetotelluric Experiment, *J. Geophys. Res.*, *116*, B02401, doi:10.1029/2010JB007740.

Nesbritt, B. E. (1993), Electrical Resistivities of Crustal Fluids, *J. Geophys. Res.*, *98*(B3), 4301–4310.

Partzsch, G. M., F. R. Schilling, and J. Arndt (2000), The influence of partial melting on the electrical behavior of crustal rocks: Laboratory examinations, model calculations and geological interpretations, *Tectonophysics*, *317*(3-4), 189–203, doi:10.1016/S0040–1951(99)00320-0.

Pollack, H. N., S. J. Hurter, and J. R. Johnson (1993), Heat flow from the Earth's interior: analysis of the global data set, *Rev. Geophys.*, *31*(3), 267–280, doi:10.1029/93RG01249.

Ren, Z. (1996), Research on the relations between Geothermal history and oil-gas accumulation in the Ordos Basin, *Acta Petrol. Sin.*, *17*(1), 17–24.

Ren, Z., S. Zhang, and S. Gao (2007), Tectonic thermal history and its significance on the formation of oil and gas accumulation and mineral deposit in Ordos Basin, *Sci. China Ser. D Earth Sci.*, *37*(S1), 23–32.

Santosh, M. (2010), Assembling North China Craton within the Columbia supercontinent: The role of double-sided subduction, *Precambrian Res.*, *178*(1-4), 149–167, doi:10.1016/j.precamres.2010.02.003.

Schwalenberg, K., V. Rath, and V. Haak (2002), Sensitivity studies applied to a two-dimensional resistivity model from the Central Andes, *Geophys. J. Int.*, *150*(3), 673–686, doi:10.1046/j.1365-246X.2002.01734.x.

Siripunvaraporn, W., G. Egbert, Y. Lenbury, and M. Uyeshima (2005), Three-dimensional magnetotelluric inversion: data-space method, *Phys. Earth Planet. Inter.*, *150*(1-3), 3–14, doi:10.1016/j.pepi.2004.08.023.

Sun, S., and S. Liu (1996), Tectono-thermal events in Ordos Basin, China, *Chin. Sci. Bull.*, *46*(24), 2870–2873.

Teng, J., et al. (2010), Velocity structure of layered block and deep dynamic process in the lithosphere beneath the Yinshan orogenic belt and Ordos Basin, *Chin. J. Geophys.*, *53*(1), 67–85.

Tian, X., J. Teng, H. Zhang, Z. Zhang, and Y. Zhang (2011), Structure of crust and upper mantle beneath the Ordos Block and the Yinshan Mountains revealed by receiver function analysis, *Phys. Earth Planet. Inter.*, *184*(3-4), 186–193, doi:10.1016/j.pepi.2010.11.007.

Wang, D., M. Mookherjee, Y. Xu, and S. Karato (2006), The effect of water on the electrical conductivity of olivine., *Nature*, *443*(7114), 977–80, doi:10.1038/nature05256.

Wang, X., Y. Zhan, G. Zhao, L. Wang, and J. Wang (2010), Deep electric structure beneath the north section of the west margin of the Ordos Basin, *Chin. J. Geophys.*, *53*(3), 595–604.

Wannamaker, P. E., et al. (2008), Lithospheric dismemberment and magmatic processes of the Great Basin–Colorado Plateau transition, Utah, implied from magnetotellurics, *Geochem. Geophys. Geosyst.*, *9*(5), Q05019, doi:10.1029/2007GC001886.

Wannamaker, P. E., T. G. Caldwell, G. R. Jiracek, V. Maris, G. J. Hill, Y. Ogawa, H. M. Bibby, S. L. Bennie, and W. Heise (2009), Fluid and deformation regime of an advancing subduction system at Marlborough, New Zealand., *Nature*, *460*(7256), 733–736, doi:10.1038/nature08204.

Wei, W., et al. (2001), Detection of widespread fluids in the Tibetan crust by magnetotelluric studies, *Science*, *292*, 716–719.

Xiao, W., B. Windley, J. Hao, and M. Zhai (2003), Accretion leading to collision and the Permian Solonker suture, Inner Mongolia, China: Termination of the central Asian orogenic belt, *Tectonics*, *22*(6), 1069, doi:10.1029/2002TC001484.

Yoshino, T., M. Laumonier, E. McIsaac, and T. Katsura (2010), Electrical conductivity of basaltic and carbonatite melt-bearing peridotites at high pressures: Implications for melt distribution and melt fraction in the upper mantle, *Earth Planet. Sci. Lett.*, *295*(3-4), 593–602, doi:10.1016/j.epsl.2010.04.050.

Yuan, Y., S. Hu, H. Wang, and F. Sun (2007), Meso-Cenozoic tectonothermal evolution of Ordos Basin, central China: Insights from newly acquired vitrinite reflectance data and a revision of existing paleothermal indicator data, *J. Geodyn.*, *44*(1-2), 33–46, doi:10.1016/j.jog.2006.12.002.

Zang, S. X., R. Qiang Wei, and Y. G. Liu (2005), Three-dimensional rheological structure of the lithosphere in the Ordos Block and its adjacent area, *Geophys. J. Int.*, *163*(1), 339–356, doi:10.1111/j.1365-246X.2005.02745.x.

Zhang, F. Q., J. Z. Liu, and Z. Y. Ouyang (1998), Tectonic framework of greenstones in the basement of the North China Craton, *Acta Geophys. Sin.*, *41*, 99–107.

Zhang, Z., Y. Wang, Y. Chen, G. a. Houseman, X. Tian, E. Wang, and J. Teng (2009), Crustal structure across Longmenshan fault belt from passive source seismic profiling, *Geophys. Res. Lett.*, *36*, L17310, doi:10.1029/2009GL039580.

Zhao, G., S. a. Wilde, P. a. Cawood, and M. Sun (2001), Archean blocks and their boundaries in the North China Craton: lithological, geochemical, structural and P–T path constraints and tectonic evolution, *Precambrian Res.*, *107*(1-2), 45–73, doi:10.1016/S0301–9268(00)00154-6.

Zhao, G., M. Sun, S. a. Wilde, and L. Sanzhong (2005), Late Archean to Paleoproterozoic evolution of the North China Craton: Key issues revisited, *Precambrian Res.*, *136*(2), 177–202, doi:10.1016/j.precamres.2004.10.002.

Zhao, G., Y. Zhan, L. Wang, J. Wang, J. Tang, X. Chen, and Q. Xiao (2011), Electrical structure of the crust beneath the Ordos Block, *Earthquake Res. China*, *25*(2), 121–134.

Zhao, L., R. M. Allen, T. Zheng, and S.-H. Hung (2009), Reactivation of an Archean craton: Constraints from P- and S-wave tomography in North China, *Geophys. Res. Lett.*, *36*, L17306, doi:10.1029/2009GL039781.

Zhao, L., R. M. Allen, T. Zheng, and R. Zhu (2012), High-resolution body wave tomography models of the upper mantle beneath eastern China and the adjacent areas, *Geochem. Geophys. Geosyst.*, *13*, Q06007, 1–20, doi:10.1029/2012GC004119.

Zhu, R., Y. Xu, G. Zhu, H. Zhang, Q. Xia, and T. Zheng (2012), Destruction of the North China Craton, *Sci. China Earth Sci.*, *55*(10), 1565–1587, doi:10.1007/s11430-012-4516-y.